Article:
Zhang, Yue, Deng, Fujin, Hou, Jiehua et al. (5 more authors) (2022) Cascaded Modular Multilevel Converter and Cycloconverter Based Machine Drive System. IEEE Transactions on Industrial Electronics. ISSN 0278-0046

https://doi.org/10.1109/TIE.2022.3169851

Cascaded Modular Multilevel Converter and Cycloconverter Based Machine Drive System

Yue Zhang, Fujin Deng, *Senior Member*, *IEEE*, Jiehua Hou, Pengyuan Jiang, Hanlu Zhang, Kangshun Zhu, Yihua Hu, *Senior Member*, *IEEE* and Sergio Vazquez, *Fellow*, *IEEE*

***Abstract*— Low-speed drive is one of the challenges for modular multilevel converters (MMCs) due to large capacitor voltage fluctuation. In this paper, a cascaded MMC and cycloconverter (CCV) based machine drive system is proposed to ensure stable operation of medium--voltage and low-speed machine. The MMC provides medium-frequency ac voltage for the CCV, and the CCV converts the medium-frequency ac input to low-frequency ac output required by the machine. Detailed analysis about MMC's operation frequency, device current stress and submodule (SM) capacitance are given in this paper. Proposed drive system can operate at zero/low frequency under rated load torque, while the SM capacitance is much smaller than that in existing methods. Simulation and experimental studies are conducted, and the results verify the effectiveness of proposed system.**

***Index* Terms— Capacitor voltage, cycloconverter, low-speed machine drive, modular multilevel converter (MMC).**

I. INTRODUCTION

The modular multilevel converter (MMC), which was firstly proposed in 2003 [1], has become the most potential topology for next-generation medium/high-voltage applications due to its advantages such as modularity, high efficiency, and flexible expandability [2]-[7]. In recent years, the MMC is attractive for the medium-voltage drive applications.

The submodule (SM) capacitor voltage fluctuation is one of the important issues for the MMC working at low frequency. The voltage fluctuation is inversely proportional to the operation frequency of the MMC [8]. For the MMC's zero/low-speed high-torque scenarios such as hoister, conveyor and mill applications, the voltage fluctuation will be large and unacceptable, which would cause overmodulation and degrades the system reliability [9].

To date, the mainstream solution to suppress the capacitor voltage fluctuation in the MMC at low speed is the current injection based methods [10]-[14]. Kolb *et al*. [10] presents the injection of high-frequency sinusoidal common-mode voltage and circulating current, which can eliminate the low-frequency capacitor voltage fluctuation, but the device current stress is increased [11]. To reduce the device current stress, the improved injection methods [12]-[14] are proposed for the MMC. However, the injection of high-amplitude current is still needed. The current injection based methods require to inject high-amplitude circulating current and the device current stress is extremely high especially in low-speed high-torque scenarios.

Alternatively, the capacitor voltage fluctuation in the MMC at low speed can be reduced by variable dc voltage methods [15]-[21]. Li *et al*. [15] proposes a hybrid MMC (HMMC) with a chopper on the dc side, which can change the average dc voltage along with the variation of output frequency. However, the average dc voltage cannot be reduced to zero, so the voltage fluctuation is still high at zero/low speed. Sau *et al*. [16] applies parallel SMs in [17], then the MMC operates with one SM in each arm at zero/low speed. However, the output voltage of parallel SMs is limited, which cannot satisfy the operation for medium-voltage low-speed machines. Kumar *et al*. [18] and [19] use a back-to-back (BTB) MMC, where the grid-side MMC is controlled as a current source, and the capacitor voltage fluctuation keeps unchanged. However, both the grid-side and machine-side MMCs require full-bridge SMs, which greatly increases the number of devices. Although Guan *et al*. [20] and Li *et al*. [21] reduce the devices of BTB-MMCs, the stable operation under rated torque at zero speed cannot be ensured. The variable dc voltage methods have limitation to suppress the capacitor voltage fluctuation of MMCs for medium-voltage low-speed drive, which require large SM capacitance [15], [18].

This paper proposes a cascaded MMC and cycloconverter (CCV) based machine drive system for the medium-voltage low-speed machine, which extends the work in [22]. Detailed analysis is conducted in this paper, including the operation frequency of MMCs, device current stress, and SM capacitance. In addition, a prototype of the proposed machine drive system is built in the lab and the experimental studies are conducted in this paper. In the proposed system, the MMC operates at medium frequency, providing constant ac voltage for the CCV, and the CCV converts the medium-frequency ac input to low-frequency ac output required by the machine. The paper includes following contributions: 1) the proposed drive system can operate at zero/low frequency under rated load torque; 2) the MMC in the proposed drive system operates at medium frequency, which requires smaller SM capacitance compared to variable dc voltage methods [15]-[21]; 3) the device current

This work was supported in part by the National Natural Science Foundation of China under Project 61873062. *(Corresponding author: Fujin Deng.)*

Y. Zhang, J. Hou, P. Jiang, H. Zhang and K. Zhu are with the School of Electrical Engineering, Southeast University, Nanjing 210096, China (e-mail: zhang_y@seu.edu.cn; 220202926@seu.edu.cn; 220192735 @seu.edu.cn; 220202933@seu.edu.cn; 220202935@seu.edu.cn).

F. Deng is with the School of Electrical Engineering, Southeast University, and Jiangsu Key Laboratory of Smart Grid Technology and Equipment, Nanjing 210096, China (e-mail: fdeng@seu.edu.cn).

Y. Hu is with the Department of Electronic Engineering, University of York, York, YO10 5DD, U.K. (e-mail: yihua.hu@york.ac.uk).

S. Vazquez is with the Department of Electronic Engineering, University of Seville, 41092 Seville, Spain (e-mail: sergi@us.es).

stress in the MMC with proposed method is much less than that with current injection based methods [10]-[14].

The rest of paper is organized as follows. Section II proposes the cascaded MMC and CCV based machine drive system. Section III proposes operating principles. Section IV discusses the proposed system. Sections V and VI present the simulation and experiment, respectively. Section VII gives conclusion.

II. Proposed Cascaded MMC and CCV Based Machine Drive System

A. Proposed Drive System

A cascaded MMC and CCV based machine drive system is proposed, as shown in Fig. 1. The MMC operates as the grid-side converter, and the CCV operates as the machine-side converter. The MMC is connected to the dc grid and provides the ac voltage with medium-frequency f_g for the CCV. The CCV converts the input medium-frequency ac voltage to the required ac voltage with low-frequency f_m to drive the permanent magnet synchronous machine (PMSM).

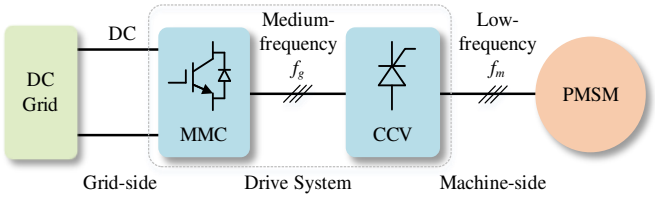

Fig. 1. Block diagram of proposed machine drive system.

B. MMC Based Grid-Side Converter

Fig. 2(a) shows the grid-side three-phase MMC, whose each phase includes an upper arm, a lower arm, a filter inductor L_f, and a compensation capacitor C_{com}. Each arm consists of n identical SMs and an arm inductor L_s. Fig. 2(b) shows a SM, which consists of the switch/diode T_1/D_1, T_2/D_2 and a dc capacitor C_{sm}.

According to [5], in the MMC, the output voltage u_j in phase j (j=a, b, c) can be expressed as

$$u_j = \frac{u_{lj} - u_{uj}}{2} - L\frac{di_j}{dt} \tag{1}$$

with

$$L = \frac{L_s}{2} + L_f \tag{2}$$

where u_{uj} and u_{lj} are the total SM output voltage of the upper arm and lower arm in phase j, respectively. i_j is the ac-side current of phase j. L is the equivalent output inductance of the MMC.

C. CCV Based Machine-Side Converter

Fig. 3 shows the machine-side three-pulse half-wave CCV. The CCV consists of three phase units. Each phase unit contains three pairs of inverse parallel thyristors including Th_{p1} & Th_{n1}, Th_{p2} & Th_{n2}, and Th_{p3} & Th_{n3}, where the thyristors Th_{p1}-Th_{p3} constitute a positive converter and the thyristors Th_{n1}-Th_{n3} constitute a negative converter. L_T is the commutation inductor.

Taking phase unit a for example and neglecting harmonics, Fig. 4 shows the fundamental components of the output voltage

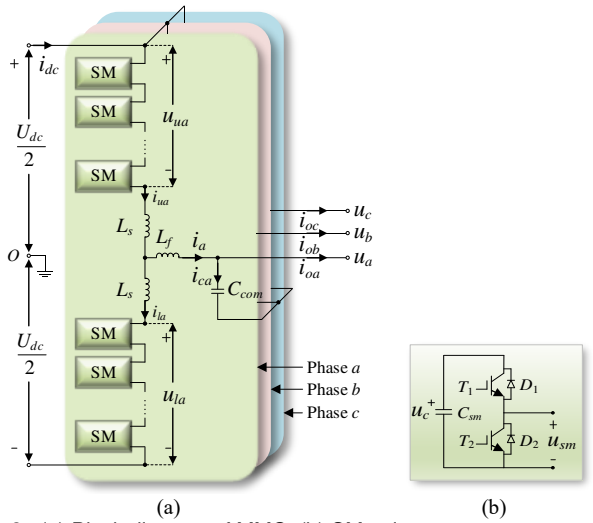

Fig. 2. (a) Block diagram of MMC. (b) SM unit.

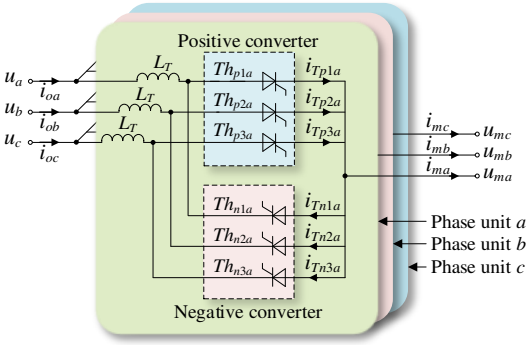

Fig. 3. Block diagram of the CCV.

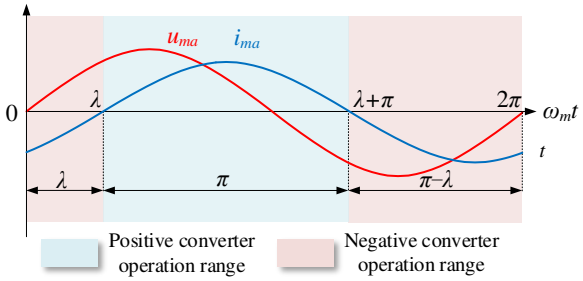

Fig. 4. Fundamental frequency components of the CCV's output.

u_{ma} and current i_{ma} of the CCV, which can be expressed as

$$u_{ma} = U_m \sin(\omega_m t) \tag{3}$$

$$i_{ma} = I_m \sin(\omega_m t - \lambda) \tag{4}$$

where U_m and I_m are the amplitudes of the machine phase voltage and current, respectively. ω_m is the fundamental angular frequency. λ is the lagging displacement angle of machine, which decides the operation of the positive converter and negative converter, as follows.

- $\omega_m t \in [\lambda, \lambda+\pi]$: i_{ma} is positive and the positive converter (Th_{p1a}, Th_{p2a}, Th_{p3a}) works.
- $\omega_m t \in [0, \lambda]$ & $[\lambda+\pi, 2\pi]$: i_{ma} is negative and the negative converter (Th_{n1a}, Th_{n2a}, Th_{n3a}) works.

The Th_{p1a}, Th_{p2a}, Th_{p3a} in the positive converter or the Th_{n1a}, Th_{n2a}, Th_{n3a} in the negative converter are fired alternately, and only one thyristor is conducting simultaneously, where the thyristor's firing angle α can be obtained based on the cosine

wave crossing method [23], as

$$\alpha = \arccos(y_{ref\_ma}) \tag{5}$$

with

$$y_{ref\_ma} = r \cdot \sin(\omega_m t) \tag{6}$$

where y_{ref_ma} is the reference for phase a of the CCV. r is modulation index with $0 \le r \le 1$.

III. Control of Proposed Machine Drive System

A. Control of Grid-Side MMC

The MMC provides a constant medium-frequency ac output voltage for the CCV. The control structure of the MMC is shown in Fig. 5(a), including the output voltage control and circulating current suppression control (CCSC) [24]. Fig. 5(b) shows the output voltage control in detail, which adopts double-loop vector control to ensure a constant output voltage of the MMC. u_d, u_q and i_{od}, i_{oq} are the dq-axis components of output voltages u_a, u_b, u_c and output currents i_{oa}, i_{ob}, i_{oc}, respectively. i_d, i_q are the dq-axis components of ac-side currents i_a, i_b, i_c. ω_g is the angular frequency of output voltage and $\omega_g = 2\pi f_g$, where f_g is the MMC's output frequency. U_{dc} is the dc-side voltage of the MMC. According to the voltage commands u_d^* and u_q^*, where u_d^* is equal to the amplitude of MMC's phase voltage and u_q^* is 0, the outer loop generates the current commands i_d^* and i_q^*. The inner loop produces the dq-axis reference voltages u_{ref_d} and u_{ref_q}. And then, the reference voltage u_{ref_j} for phase j is derived by the inverse dq transformation. Fig. 5(c) shows the CCSC in detail, i_{uj} and i_{lj} are the upper and lower arm currents in phase j, respectively. i_{cir_d} and i_{cir_q} are the dq-axis components of circulating currents, respectively. The CCSC produces the dq-axis reference voltages u_{cir_d} and u_{cir_q}, then the reference voltage u_{cir_j} for phase j is derived by the inverse dq transformation. Finally, the upper arm reference voltage and lower arm reference voltage can be obtained as $u_{ref\_uj} = (u_{cir\_j} - u_{ref\_j})$ and $u_{ref\_lj} = (u_{cir\_j} + u_{ref\_j})$, where the u_{cir_j} is the reference for phase j produced by the CCSC, as shown in Fig. 5(a). Finally, the upper arm reference and lower arm reference signals can be obtained as

$$\begin{cases} y_{ref\_uj} = 2u_{ref\_uj}/U_{dc} \\ y_{ref\_lj} = 2u_{ref\_lj}/U_{dc} \end{cases} \tag{7}$$

which are used for the upper arm and the lower arm in phase j of the MMC, respectively.

B. Control of Machine-Side CCV

The CCV is employed to control the machine and Fig. 6 shows the vector control of the CCV. i_{md}, i_{mq} and L_{md}, L_{mq} are the dq-axis components of machine currents and inductances, respectively. ψ is the permanent magnet flux linkage. θ is the electrical rotor position angle of the machine. According to the command ω_m^*, the outer loop produces the q-axis current command i_{mq}^*. The d-axis current command i_{md}^* is 0. The inner loop produces the dq-axis reference voltages u_{ref_md} and u_{ref_mq} to make the current i_{md} and i_{mq} follow their commands, and then three-phase reference voltage u_{ref_mj} is derived from the inverse dq transformation. According to [23], the relationship among

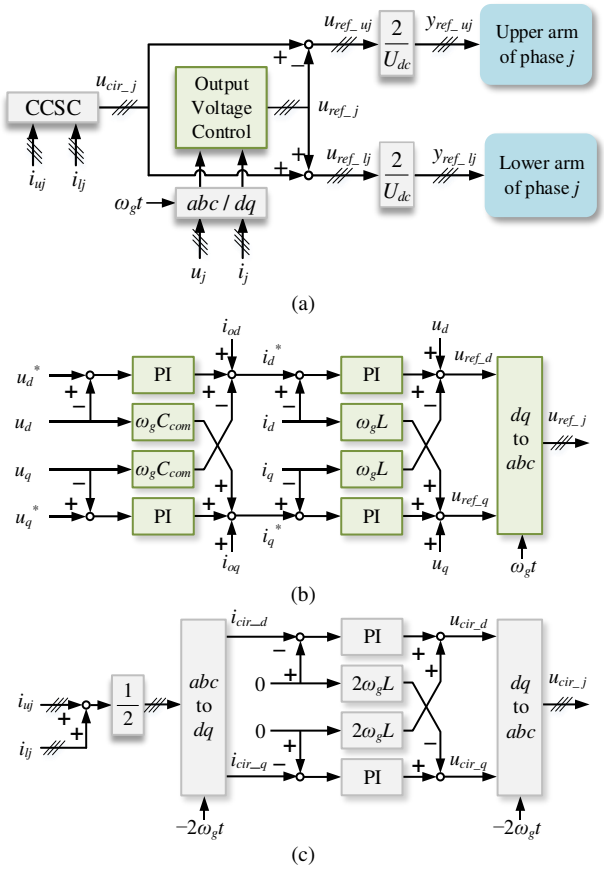

Fig. 5. (a) Overall control diagram of the grid-side MMC. (b) Output voltage control diagram of the MMC. (c) Circulating current suppression control diagram of the MMC.

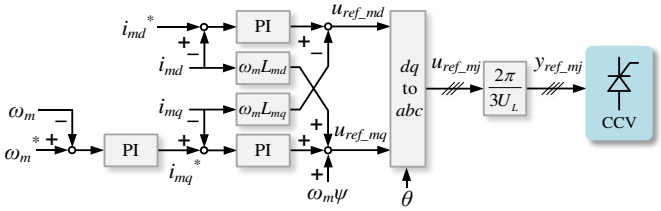

Fig. 6. Control diagram of the CCV.

CCV's input phase voltage amplitude U_P, output phase voltage amplitude U_m, and modulation index r is

$$r = \frac{2\pi U_m}{3\sqrt{3}U_P} \tag{8}$$

Substituting (8) into (6), the reference signal y_{ref_mj} can be derived as

$$y_{ref\_mj} = \frac{2\pi}{3\sqrt{3}U_P} u_{ref\_mj} = \frac{2\pi}{3U_L} u_{ref\_mj} \tag{9}$$

where U_L is the CCV's input line voltages u_{ab}, u_{bc}, u_{ca}. The y_{ref_mj} is used for the CCV to control the machine.

IV. Discussion of Proposed Drive System

A. Studied Drive System

In this paper, a 6.6 kV/5 MW low-speed PMSM based drive system is studied, which is normally operated at the rated situation in applications such as conveyor. The system parameters are shown in Table I.

TABLE I
PARAMETERS OF PROPOSED MACHINE DRIVE SYSTEM

Parameter		Value
PMSM	Rated stator rms line voltage (kV)	6.6
	Rated rms current (A)	462
	Number of pole pairs	12
	Rated speed (r/min)	50
	Rated frequency (Hz)	10
	Rated displacement factor	0.95
MMC	DC grid voltage (kV)	20
	Rated rms line voltage (kV)	8.9
	Rated frequency (Hz)	100
	SM number per arm n	12
	SM capacitance (mF)	2.76
	Arm inductance (mH)	3
	Compensation capacitance (mF)	0.1
	Carrier frequency (kHz)	1
CCV	Commutation inductance (mH)	0.63

B. Commutation Inductor L_T of CCV

The commutation inductor L_T, as shown in Fig. 3, is adopted to limit the rising rate of the CCV's thyristor current during commutation between the thyristors. Taking the commutation in the positive converter of phase unit a as an example, Fig. 7 shows the commutation from outgoing thyristor Th_{p3a} to incoming thyristor Th_{p1a} in the commutation period μ, where the Th_{p3a}'s current i_{Tp3a} is gradually reduced, the Th_{p1a}'s current i_{Tp1a} is gradually increased, and the I_T=i_{Tp1a}+i_{Tp3a} is nearly a constant. According to (4) and (5), the I_T can be obtained as

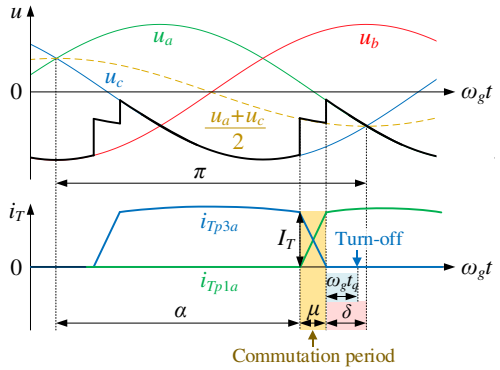

Fig. 7. Commutation from Th_{p3a} to Th_{p1a}.

$$I_T = I_m \sin\left[\arcsin\left(\frac{\cos\alpha}{r}\right)-\lambda\right] \tag{10}$$

The rising rate of the thyristor current i_T during commutation period μ is

$$\frac{di_T}{dt}=2\pi f_g \cdot \frac{I_T}{\mu} \tag{11}$$

with

$$\mu=\arccos\left(\cos\alpha-\frac{4\pi f_g L_T I_T}{U_L}\right)-\alpha \tag{12}$$

It can be observed that along with the increase of the commutation inductor L_T, the di_T/dt will reduce; along with the reduction of L_T, the di_T/dt will increase.

Normally, the maximum di_T/dt appears when the CCV works at the rated situation. According to (10) and (11), the di_T/dt is related to α for the given L_T and f_g. Fig. 8(a) shows the range of α for the positive converter in phase unit a under various phase angle $\omega_m t$ of u_{ma}, which is derived from Table I. Fig. 8(b) shows the di_T/dt under various phase angles $\omega_m t$ of u_a and various f_g, where L_T=0.63 mH. It can be observed that the di_T/dt reaches its minimum value when phase angle $\omega_m t$ is close to $\pi/2$, and the di_T/dt increases when the $\omega_m t$ is far from $\pi/2$. The maximum di_T/dt under various f_g are all close to 10 A/μs. Taking the thyristor Infineon T2871N [25] as an example, whose nominal di_T/dt is 10 A/μs. In order to ensure that the maximum di_T/dt does not exceed the nominal value, L_T should be more than 0.63 mH.

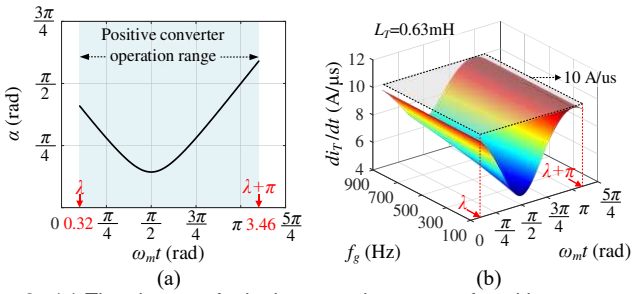

Fig. 8. (a) The change of α in the operation range of positive converter. (b) di_T/dt under various f_g when L_T=0.63 mH.

C. Operation Frequency f_g of MMCs

In Fig. 7, the extinction angle δ is

$$\delta=\pi-(\alpha+\mu) \tag{13}$$

The extinction time t_δ is

$$t_\delta=\frac{\delta}{2\pi}\cdot\frac{1}{f_g} \tag{14}$$

According to (13) and (14), it can be observed that along with the increase of (α+μ) and f_g, the t_δ will reduce, which is critical for the commutation. According to (5) and (12), (α+μ) can reach the maximum at rated power, which will result in the minimum δ. Taking the positive converter in phase unit a as an example, and according to (14), Fig. 9(a) shows the t_δ in the operation range of positive converter under rated situation, where various f_g are considered. Based on Fig. 9(a), the minimum extinction time t_{δ_min} under various f_g can be obtained, as shown in Fig. 9(b). Along with the increase of f_g, the t_{δ_min} will reduce, and vice versa.

In order to avoid commutation failure, the minimum t_{δ_min} of the thyristor must be more than the thyristor's turn-off time t_q. As a result, according to Fig. 9(b), the maximum f_g should meet

$$f_{g\_max} \le f_g\big|_{(t_{\delta\_min}=t_q)} \tag{15}$$

The minimum f_g of CCV is limited by its output frequency f_m. Referring to [26], the minimum f_g in three-pulse half-wave CCV should be

$$f_{g\_min} \ge 6 f_m \tag{16}$$

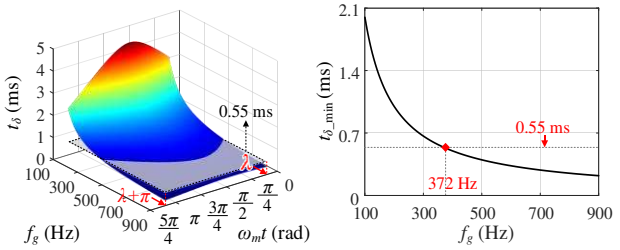

(a) (b)

Fig. 9. (a) t_δ under various f_g in the operation range of positive converter. (b) t_{δ_min} under various f_g.

For the system in Table I, the thyristor Infineon T2871N [25] is considered, whose t_q is 0.55 ms. According to Fig. 9(b) and (15), there is f_{g_max}≤372 Hz. The rated frequency f_m of the machine is 10 Hz. According to (16), there is f_{g_min}≥60 Hz. Although a higher f_g brings smoother output current, it requires higher sampling frequency. Here, the rated f_g is set as 100 Hz.

D. Compensation Capacitor C_{com} of MMCs

A compensation capacitor C_{com}, as shown in Fig. 2, is adopted in the MMC, whose capacitive reactive power is

$$Q_{NC}=\frac{1}{2}\omega_g C_{com}U_L^2 \tag{17}$$

The C_{com} is used to compensate the inductive reactive power Q_{NV} of the CCV at rated situation, which is caused by the CCV and results in the lagging displacement angle φ_N between the CCV's input currents i_{oa}, i_{ob}, i_{oc} and phase voltages u_a, u_b, u_c. Here, the inductive reactive power Q_{NV} of the CCV at rated can be calculated as

$$Q_{NV}=P_{NV}\tan\varphi_N \tag{18}$$

where P_{NV} is the rated power at the input side of the CCV. Neglecting the power loss in the CCV, the P_{NV} equals to the rated power at the ac side of the machine as

$$P_{NV}=\frac{3}{2}U_{mN}I_{mN}\cos\lambda \tag{19}$$

where U_{mN} and I_{mN} are the amplitude of machine's rated phase voltage and current, respectively.

According to (17)~(18), the C_{com} can be obtained as

$$C_{com}=\frac{2P_{NV}\tan\varphi_N}{\omega_g U_L^2} \tag{20}$$

Substituting Table I into (20), the C_{com} in the system can be obtained as 0.1 mF.

E. Device Current Stress of MMCs

Suppose that the circulating current in the MMC is suppressed by the CCSC, the upper arm current i_{uj} and the lower arm current i_{lj} in phase j of the MMC, as shown in Fig. 2, can be expressed as

$$\begin{cases} i_{uj}=\dfrac{i_{dc}}{3}+\dfrac{i_j}{2} \\ i_{lj}=\dfrac{i_{dc}}{3}-\dfrac{i_j}{2} \end{cases} \tag{21}$$

where i_{dc} is the dc current. The ac-side current i_j in phase j is

$$i_j=i_{cj}+i_{oj} \tag{22}$$

with

$$i_{cj}=C_{com}\frac{du_j}{dt} \tag{23}$$

where i_{cj} is the compensation capacitor current, which mainly consists of the fundamental-frequency component. i_{oj} is the output current in phase j.

Due to the CCV, the MMC's output current i_{oj} contains fundamental-frequency component and harmonic components. Fig. 10(a) shows the frequency spectrum of i_{oj} at rated situation, which is derived from the system in Table I. It can be observed that the frequencies of the harmonics mainly include $2f_g$±$3f_m$, $4f_g$±$3f_m$, $5f_g$ & $5f_g$±$6f_m$, $7f_g$ & $7f_g$−$6f_m$. Fig. 10(b) shows the frequency spectrum of i_j at rated situation, whose harmonics are almost the same to those in i_{oj}, as shown in Fig. 10(a). The amplitude of fundamental component in Fig. 10(b) is less than that in Fig. 10(a), because its reactive component is compensated by C_{com}.

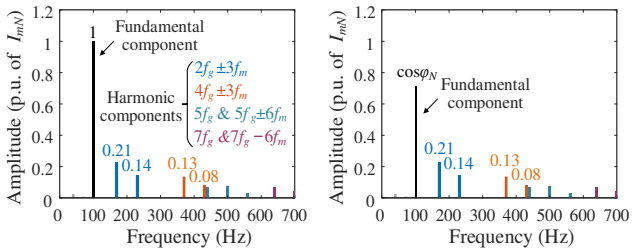

(a) (b)

Fig. 10. (a) Frequency spectrum of i_{oj} at rated situation. (b) Frequency spectrum of i_j at rated situation.

Fig. 11 shows the peak value of MMC's arm currents under various machine speeds, which is derived from the system in Table I. It can be seen that along with the increase of machine speed, the current peak value also increases. Fig. 11 also shows the current peak value of the MMC based machine drive system with square-wave circulating current injection method [11], whose current peak value is the minimum among various circulating current injection methods. It can be observed that the device current stress in the proposed machine drive system is much lower than that in the circulating current injection method, because the proposed method does not need to inject high-amplitude circulating currents.

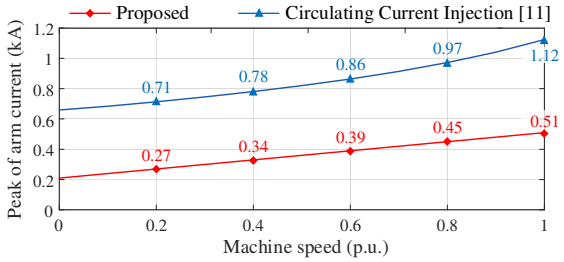

Fig. 11. Comparison of arm current peak value between proposed method and current injection method [11].

F. SM Capacitor C_{sm} of MMCs

Taking the upper arm of phase a for example, according to (21) and Fig. 10(b), the rated arm current i_{uaN} can be simplified

$$\begin{aligned}\Delta u_{cuaN}&=\frac{1}{C_{sm}}\int i_{cuaN}dt=\frac{m i_{dcN}\cos(\omega_g t)}{6\omega_g C_{sm}}-\frac{I_{mN}}{4C_{sm}\omega_g}\left\{\cos\varphi_N\cos(\omega_g t)+\frac{m\cos\varphi_N\sin(2\omega_g t)}{4}\right\}\\&=-\frac{I_{mN}}{4C_{sm}}\left\{\frac{k_{4n}}{\omega_{4n}}\cos(\omega_{4n}t+\varphi_{4n})+\frac{k_{4p}}{\omega_{4p}}\cos(\omega_{4p}t+\varphi_{4p})+\frac{k_{2p}}{\omega_{2p}}\cos(\omega_{2p}t+\varphi_{2p})+\frac{k_{2n}}{\omega_{2n}}\cos(\omega_{2n}t+\varphi_{2n})\right\}\\&\quad+\frac{m I_{mN}}{8C_{sm}}\left\{\frac{k_{2n}\sin[(\omega_{2n}+\omega_g)t+\varphi_{2n}]}{(\omega_{2n}+\omega_g)}-\frac{k_{2n}\sin[(\omega_{2n}-\omega_g)t+\varphi_{2n}]}{(\omega_{2n}-\omega_g)}+\frac{k_{2p}\sin[(\omega_{2p}+\omega_g)t+\varphi_{2p}]}{(\omega_{2p}+\omega_g)}-\frac{k_{2p}\sin[(\omega_{2p}-\omega_g)t+\varphi_{2p}]}{(\omega_{2p}-\omega_g)}\right.\\&\quad\left.+\frac{k_{4n}\sin[(\omega_{4n}+\omega_g)t+\varphi_{4n}]}{(\omega_{4n}+\omega_g)}-\frac{k_{4n}\sin[(\omega_{4n}-\omega_g)t+\varphi_{4n}]}{(\omega_{4n}-\omega_g)}+\frac{k_{4p}\sin[(\omega_{4p}+\omega_g)t+\varphi_{4p}]}{(\omega_{4p}+\omega_g)}-\frac{k_{4p}\sin[(\omega_{4p}-\omega_g)t+\varphi_{4p}]}{(\omega_{4p}-\omega_g)}\right\}\end{aligned}\tag{26}$$

as (24), where only the fundamental component and harmonic components $2f_g\pm3f_m$ and $4f_g\pm3f_m$ are considered.

$$\begin{aligned}i_{uaN}&=\frac{i_{dcN}}{3}+\frac{i_{aN}}{2}\\&=\frac{i_{dcN}}{3}+\frac{1}{2}I_{mN}\cos\varphi_N\sin(\omega_g t)\\&\quad+\frac{1}{2}I_{mN}[k_{2n}\sin(\omega_{2n}t+\varphi_{2n})+k_{2p}\sin(\omega_{2p}t+\varphi_{2p})]\\&\quad+\frac{1}{2}I_{mN}[k_{4n}\sin(\omega_{4n}t+\varphi_{4n})+k_{4p}\sin(\omega_{4p}t+\varphi_{4p})]\end{aligned}\tag{24}$$

where i_{dcN} is rated dc current. i_{aN} is the rated ac-side current of phase a. k_{2n}, k_{2p}, k_{4n}, k_{4p} are respectively the p.u. values of harmonics $2f_g-3f_m$, $2f_g+3f_m$, $4f_g-3f_m$ and $4f_g+3f_m$ as shown in Fig. 10(b). ω_{2n}, ω_{2p}, ω_{4n}, ω_{4p} are respectively the angular frequency of these harmonics. φ_{2n}, φ_{2p}, φ_{4n}, φ_{4p} are respectively the phase angles of these harmonics.

According to [27], the SM capacitor current in upper arm of phase a can be expressed as

$$i_{cuaN}=\frac{1-y_{ref\_ua}}{2}\cdot i_{uaN}\tag{25}$$

Normally, the circulating current control has little effect on the y_{ref_ua} [28]. Therefore, it can be expressed as $y_{ref\_ua}=m\cdot\sin(\omega_g t)$, where m is the modulation index of MMC. Combining (24) and (25), the rated capacitor voltage fluctuation Δu_{cuaN} can be obtained as (26).

The SM capacitor voltage fluctuation ratio ε can be defined as

$$\varepsilon=\frac{Max[\Delta u_{cuaN}]}{U_{dc}/n}\tag{27}$$

Fig. 12 shows the relationship between ε and C_{sm} in the MMC of the proposed system, which is derived from (24)~(27) and Table I. It can be seen that along with the increase of C_{sm}, ε will be reduced; along with the reduction of C_{sm}, ε will be increased. Fig. 12 also shows relationship between the ε and C_{sm} in the HMMC based machine drive system [15]. It can be observed that for the same capacitor voltage fluctuation, the required capacitance in the proposed machine drive system is far less than that in the HMMC based machine drive system. According to Fig. 12, the C_{sm} of 2.76 mF corresponding to the capacitor voltage fluctuation of 2% is selected in the proposed system.

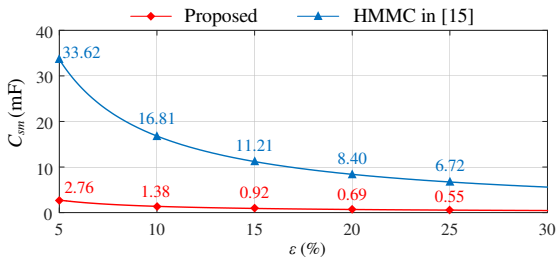

Fig. 12. Comparison of SM capacitance between MMC in proposed system and HMMC [15].

V. Simulation Studies

To verify the proposed machine drive system, the system simulation is conducted with professional tool PLECS. The system diagram is shown in Fig. 1 and the system parameters are shown in Table I.

A. Performance of proposed system

Fig. 13 shows the performance of the proposed machine drive system, where the machine operates under rated load from standstill to the rated speed. Fig. 13(a) shows the machine speed. The machine accelerates at 1s from standstill to 0.5 p.u. speed and accelerates at 2.5s from 0.5 p.u. to rated speed. Fig. 13(b) shows the machine line voltage. Fig. 13(c) shows the machine currents, whose frequency changes from 0 to 10 Hz. Fig. 13(d) shows the electrical torque. The torque ripple increases with the speed and reaches the maximum value 0.10 p.u. at rated situation. Fig. 13(e) shows the line voltages of the MMC, whose frequency f_g is 100 Hz. Fig. 13(f) shows the output current of the MMC. Fig. 13(g) shows the MMC's arm currents, whose peak value rises with with the increase of the machine speed. The peak of arm current is 514 A. Fig. 13(h) shows the SM capacitor voltages of upper and lower arm in phase a of MMC. The voltage fluctuation rises with the arm current, ranging from 1590 to 1749 V at the rated speed. The voltage fluctuation ratio is less than 5% when the C_{sm} is 2.76 mF, which verifies the analysis in Fig. 12.

Fig. 14 shows the harmonic spectrums of machine line voltage and current at rated situation. It can be observed that the main harmonic components of machine voltage are in the sidebands of $3f_g$ and $6f_g$. The main harmonic components of machine current are in the sidebands of $3f_g$.

B. Comparison with traditional MMC

Fig. 15 shows the comparison of capacitor voltages between traditional MMC based drive system and proposed system, where the SM capacitance of traditional MMC is 7 times (19.32 mF) of proposed system (2.76 mF). Fig. 15(a) and (b) show the capacitor voltage fluctuation at 0.2 p.u. speed under rated load. Fig. 15(c) and (d) show the capacitor voltage fluctuation at rated situation. It can be observed that the voltage fluctuation of

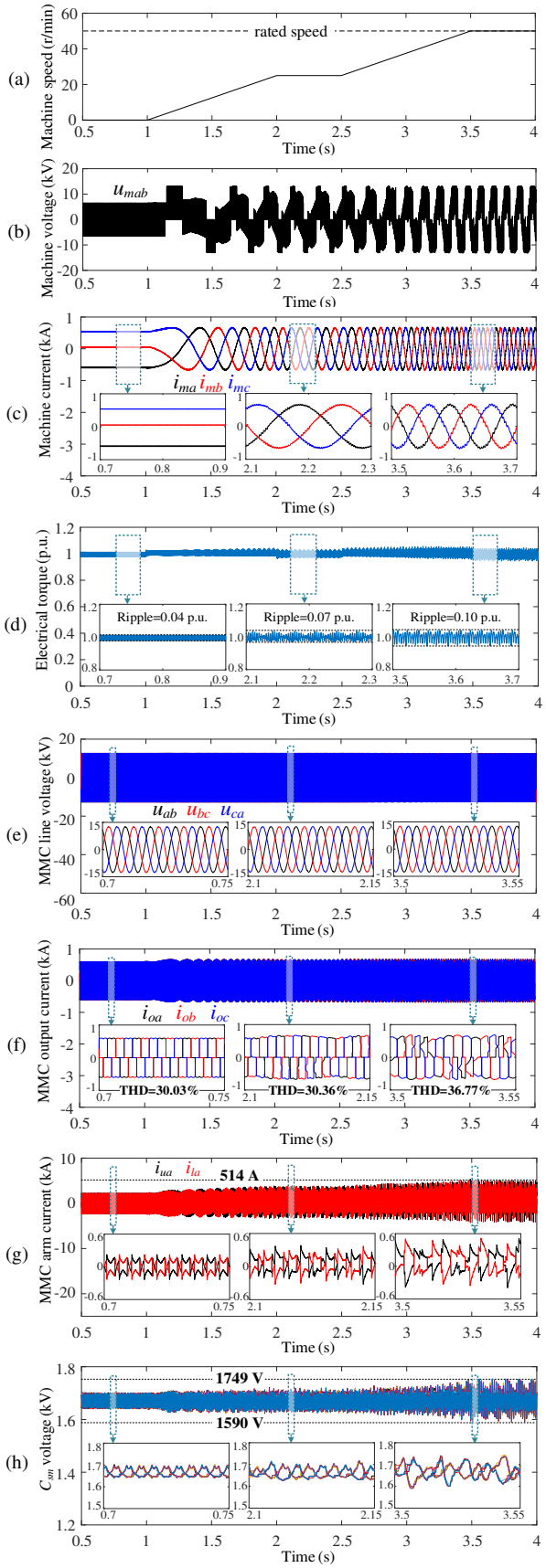

Fig. 13. Simulation waveforms. (a) Machine speed. (b) Machine line voltage. (c) Machine currents. (d) Electrical torque. (e) MMC line voltages. (f) MMC output currents. (g) Arm currents of phase a. (h) SM capacitor voltages of phase a.

traditional MMC increases as machine speed reduces, which is 42.88% at 0.2 p.u. speed. Compared to traditional MMC, proposed system can operate stably at low speed with lower SM capacitance, and the voltage fluctuation is less than 5% in the whole speed range.

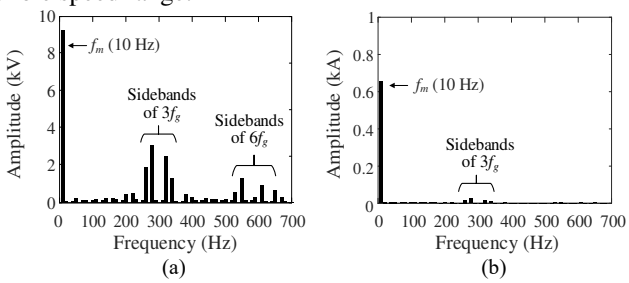

Fig. 14. Harmonic spectrum at rated situation. (a) Machine line voltage. (b) Machine current.

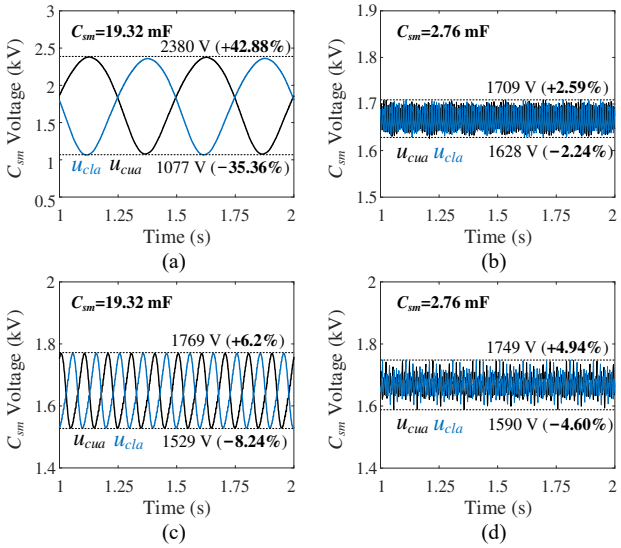

Fig. 15. Comparison of capacitor voltage fluctuation. (a) Traditional MMC at 0.2 p.u. speed. (b) Proposed system at 0.2 p.u. speed. (c) Traditional MMC at rated speed. (d) Proposed system at rated speed.

VI. Experimental Studies

A prototype of the proposed machine drive system is built in the lab, as shown in Fig. 16. A dc power supply is used to support the dc voltage. The ac side of the MMC is connected to the CCV. The output side of CCV is connected to the PMSM. The control algorithm is implemented by digital signal processor (DSP) and the drive signals are transferred to driving circuit of each device by optical fibers. The system parameters are listed in Table II.

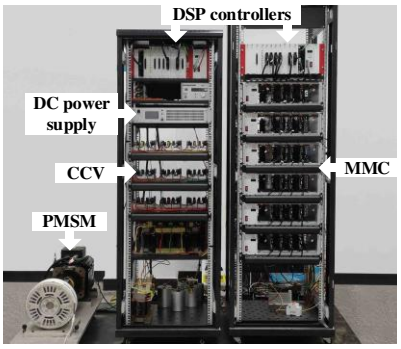

Fig. 16. Photo of experimental platform.

TABLE II
PARAMETERS OF EXPERIMENTAL SYSTEM

Parameter		Value
PMSM	Rated stator rms line voltage (V)	44
	Rated rms current (A)	5.66
	Number of pole pairs	4
	Rated speed (r/min)	150
	Rated frequency (Hz)	10
	Rated displacement factor	0.95
MMC	DC voltage (V)	140
	Rated rms line voltage (V)	62
	Rated frequency (Hz)	100
	SM number per arm n	4
	SM capacitance (mF)	2.7
	Arm inductance (mH)	0.5
	Compensation capacitance (mF)	0.18
	Carrier frequency (kHz)	5
CCV	Commutation inductance (mH)	1

A. Steady State Operation

Fig. 17 shows the shows the line voltages of the MMC, whose frequency is 100Hz. Fig. 18 shows the steady state operation at standstill under rated load. Fig. 19 shows the steady state operation at 0.5 p.u. speed under rated load. Fig. 20 shows the steady state operation at rated speed under 0.5 p.u. load. Fig. 21 shows the steady state operation at rated speed under rated load.

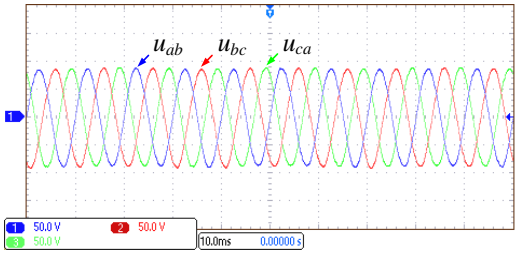

Fig. 17. Experimental waveforms of u_{ab}, u_{bc}, u_{ca} (50 V/div).

Fig. 18(a), Fig. 19(a), Fig. 20(a) and Fig. 21(a) show the machine voltages u_{mab}, u_{mbc}, u_{mca}. Fig. 18(b), Fig. 19(b), Fig. 20(b) and Fig. 21(b) show the machine currents i_{ma}, i_{mb}, i_{mc}. Under rated load in Figs. 19~20, the fundamental frequency machine current amplitude is 8 A. Under 0.5 p.u. load in Fig. 21, the fundamental frequency machine current amplitude is 4 A. Fig. 18(c), Fig. 19(c), Fig. 20(c) and Fig. 21(c) show the spectrum of machine line voltage, where the main harmonic components are in the sidebands of $3f_g$ and $6f_g$. Fig. 18(d), Fig. 19(d), Fig. 20(d) and Fig. 21(d) show the spectrum of machine current, where the main harmonic components are in the sidebands of $3f_g$. Fig. 18(e), Fig. 19(e), Fig. 20(e) and Fig. 21(e) show the MMC's output current i_{oa}, i_{ob}, i_{oc}, whose THD reaches the maximum 34.06% at rated situation. Fig. 18(f), Fig. 19(f), Fig. 20(f) and Fig. 21(f) show the arm currents and the SM capacitor voltages in phase a of the MMC. It can be observed that the peak of arm current increases as the machine speed and torque increase. At rated situation, the peak of arm current

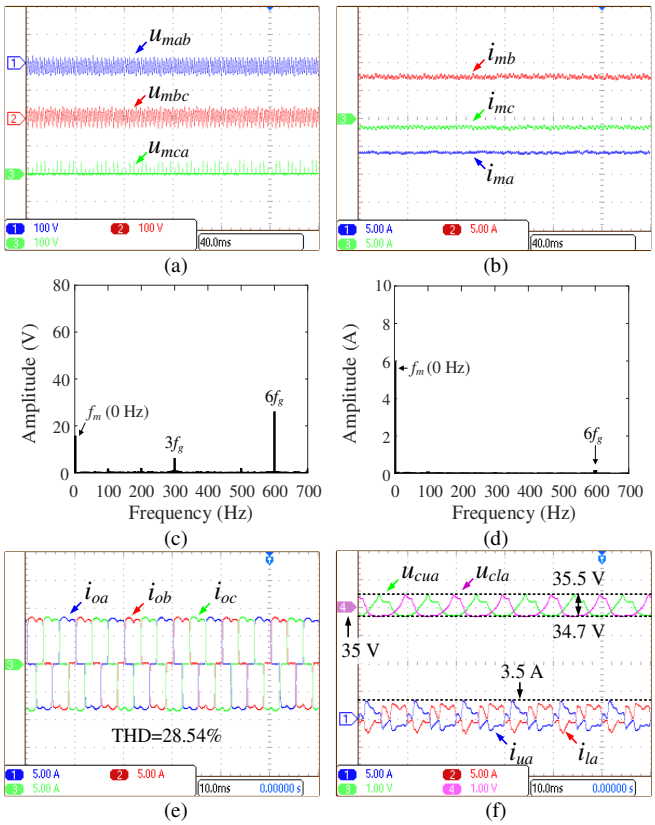

Fig. 18. Experimental waveforms at standstill. (a) u_{mab}, u_{mbc}, u_{mca} (100 V/div). (b) i_{ma}, i_{mb}, i_{mc} (5 A/div). (c) Spectrum of u_{mab}. (d) Spectrum of i_{ma}. (e) i_{oa}, i_{ob}, i_{oc} (5 A/div). (f) i_{ua}, i_{la}, (5 A/div), u_{cua}, u_{cla} (1 V/div).

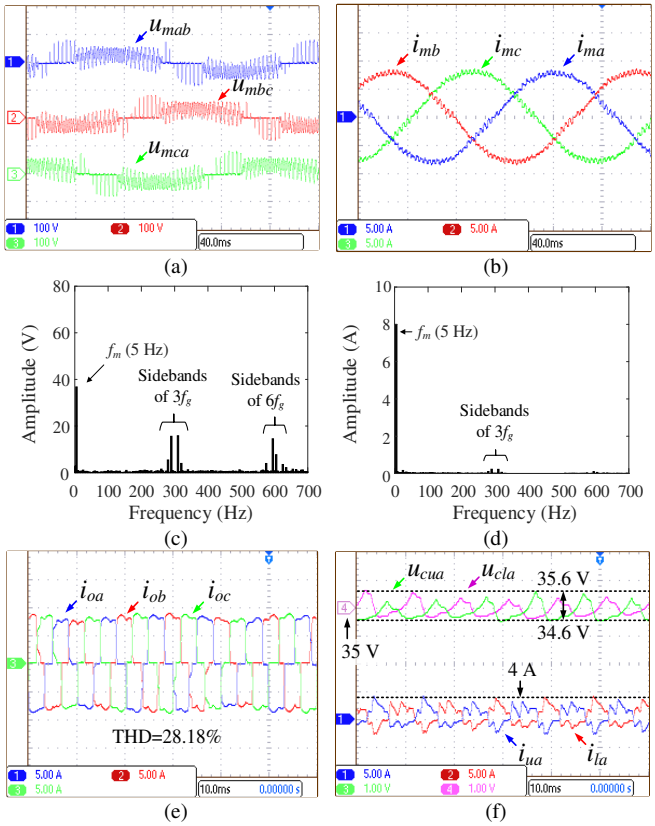

Fig. 19. Experimental waveforms at 0.5 p.u. speed. (a) u_{mab}, u_{mbc}, u_{mca} (100 V/div). (b) i_{ma}, i_{mb}, i_{mc} (5 A/div). (c) Spectrum of u_{mab}. (d) Spectrum of i_{ma}. (e) i_{oa}, i_{ob}, i_{oc} (5 A/div). (f) i_{ua}, i_{la}, (5 A/div), u_{cua}, u_{cla} (1 V/div).

This article has been accepted for publication in a future issue of this journal, but has not been fully edited. Content may change prior to final publication. Citation information: DOI 10.1109/TIE.2022.3169851, IEEE Transactions on Industrial Electronics

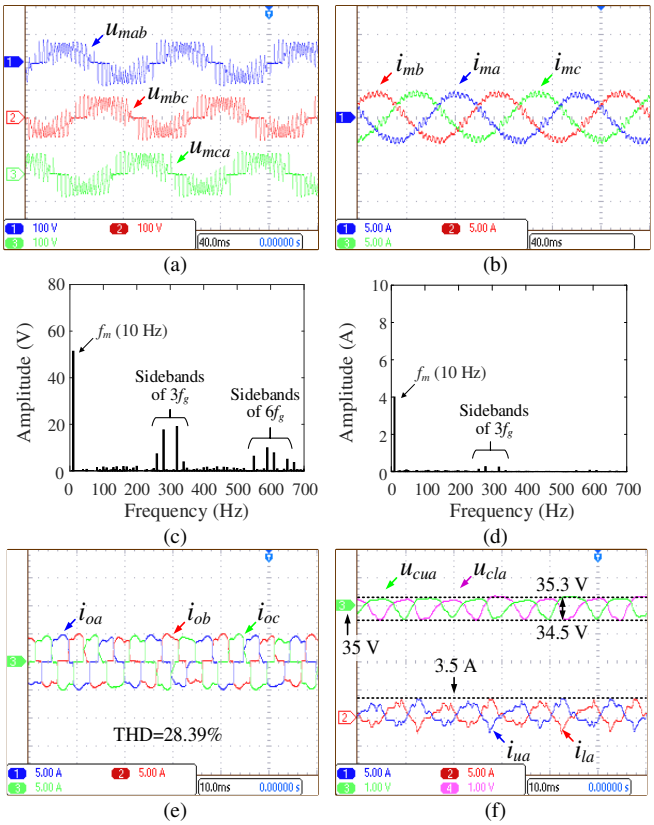

Fig. 20. Experimental waveforms under 0.5 p.u. load. (a) u_{mab}, u_{mbc}, u_{mca} (100 V/div). (b) i_{ma}, i_{mb}, i_{mc} (5 A/div). (c) Spectrum of u_{mab}. (d) Spectrum of i_{ma}. (e) i_{oa}, i_{ob}, i_{oc} (5 A/div). (f) i_{ua}, i_{la}, (5 A/div), u_{cua}, u_{cla} (1 V/div).

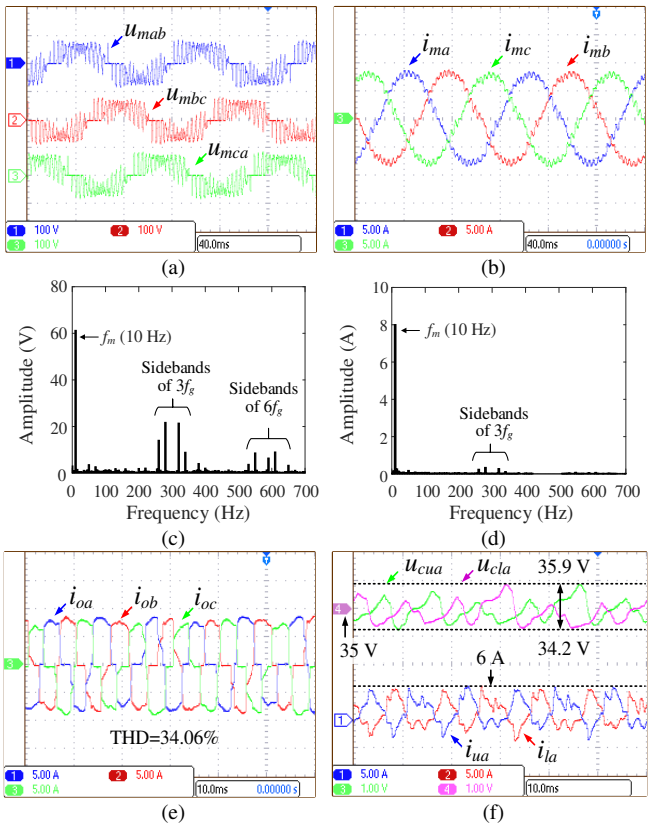

Fig. 21. Experimental waveforms at rated situation. (a) u_{mab}, u_{mbc}, u_{mca} (100 V/div). (b) i_{ma}, i_{mb}, i_{mc} (5 A/div). (c) Spectrum of u_{mab}. (d) Spectrum of i_{ma}. (e) i_{oa}, i_{ob}, i_{oc} (5 A/div). (f) i_{ua}, i_{la}, (5 A/div), u_{cua}, u_{cla} (1 V/div).

reaches the maximum 6 A.

The SM capacitor voltage fluctuation also increases as the machine speed and torque increase. At rated situation, the voltage fluctuation reaches the upper limit, which ranges from 34.2 to 35.9 V. The voltage fluctuation ratio ε is 2.57% under the C_{sm} of 2.7 mF. According to (24)~(27) and experiment parameters in Table II, Fig. 22 shows the required C_{sm} under various ε. The estimated ε is 2.6% when C_{sm} is 2.7 mF, and accordingly the experimental result is almost consistent with the theoretical analysis.

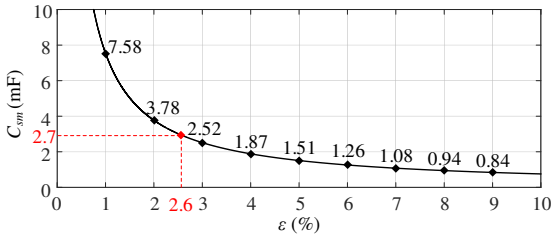

Fig. 22. Theoretical analysis of voltage fluctuation ratio under experimental parameters.

Fig. 23 shows the machine torque ripple at different operation situation. It can be observed that the torque ripple reaches the upper limit at rated situation, which is 0.12 p.u. as shown in Fig. 23(d).

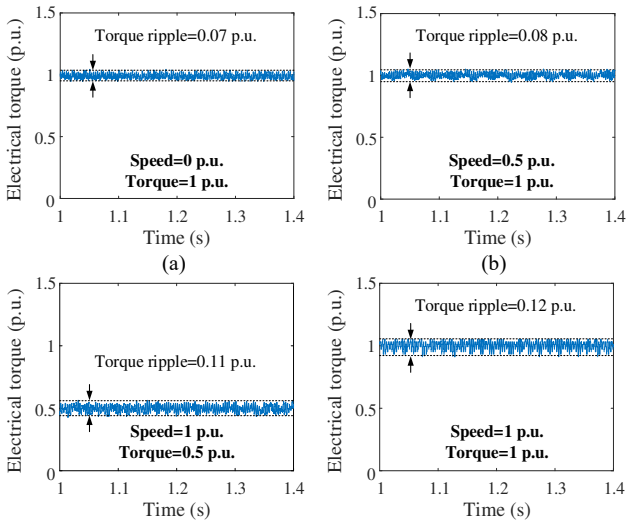

Fig. 23. Electrical torque in the experiment. (a) Electrical torque at standstill under rated load. (b) Electrical torque at 0.5 p.u. speed under rated load. (c) Electrical torque at rated speed under 0.5 p.u. load. (d) Electrical torque at rated situation.

B. Dynamic Performance

Fig. 24 shows the dynamic performance when the machine operates from standstill to the rated frequency (10Hz) under rated load. Fig. 24(a) shows the machine line voltages u_{mab}, u_{mbc}, u_{mca}. Fig. 24(b) shows the machine currents i_{ma}, i_{mb}, i_{mc}, whose fundamental frequency amplitude is 8 A. Fig. 24(c) shows the MMC's output currents i_{oa}, i_{ob}, i_{oc}. Fig. 24(d) shows the arm currents and the SM capacitor voltages in phase a of the MMC. The peak of arm current increases with the machine speed, and its maximum value is 6 A. The voltage fluctuation of SM capacitors rises with the speed, and the maximum voltage fluctuation ratio is 2.57%.

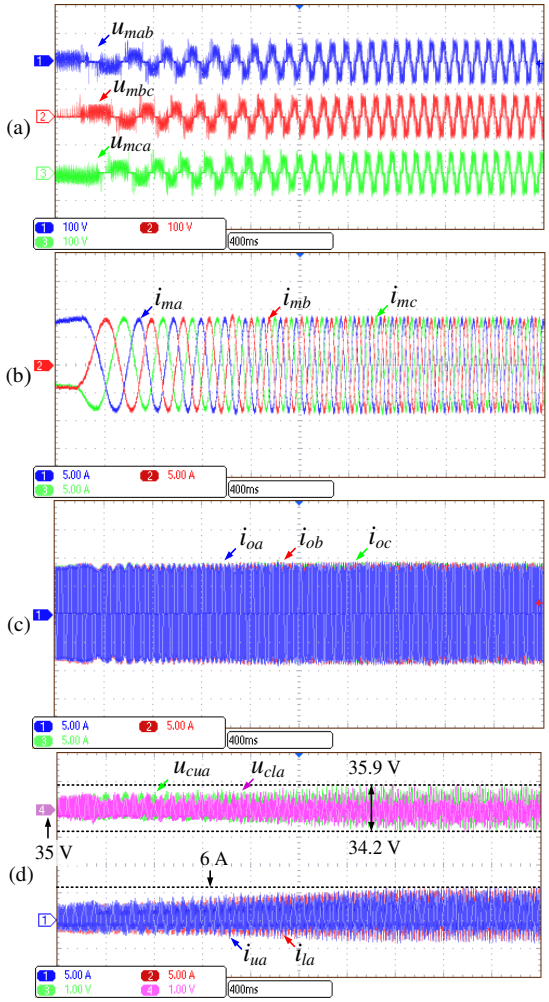

Fig. 24. Experimental waveforms when the system operates from standstill to rated speed. (a) u_{mab}, u_{mbc}, u_{mca} (100 V/div). (b) i_{ma}, i_{mb}, i_{mc} (5 A/div). (c) i_{oa}, i_{ob}, i_{oc} (5 A/div). (d) i_{ua}, i_{la}, (5 A/div), u_{cua}, u_{cla} (1 V/div).

VII. Conclusion

This paper proposes a cascaded MMC and CCV based machine drive system, which can operate stably at zero/low frequency. In the proposed system, the MMC operates at the medium frequency, providing constant ac voltage for the CCV. The CCV converts the medium-frequency ac input to low-frequency ac output required by the machine. The range of MMC's operation frequency is analyzed based on the safety commutation of thyristors in the CCV. Considering the fundamental and harmonic components of MMC's output current, the device current stress in the MMC is analyzed. The SM capacitance is also analyzed, which is significantly smaller than the existing MMC based methods. Simulation and experiment are conducted and their results verify the effectiveness of proposed machine drive system.

References

[1] M. Huang, J. Zou, and X. Ma, "An improved phase-shifted carrier modulation for modular multilevel converter to suppress the influence of fluctuation of capacitor voltage," *IEEE Trans. Power Electron.*, vol. 31, no. 10, pp. 7404–7416, Oct. 2016.

[2] J. I. Leon, S. Vazquez and L. G. Franquelo, "Multilevel Converters: Control and Modulation Techniques for Their Operation and Industrial Applications," *Proc. IEEE*, vol. 105, no. 11, pp. 2066-2081, Nov. 2017.

[3] C. Liu, F. Deng, Q. Heng, X. Cai, R. Zhu and M. Liserre, "Crossing Thyristor Branches-Based Hybrid Modular Multilevel Converters for DC Line Faults," *IEEE Trans. Ind. Electron*, vol. 68, no. 10, pp. 9719-9730, Oct. 2021.

[4] F. Deng *et al*., "Temperature-Balancing Control for Modular Multilevel Converters under Unbalanced Grid Voltages," *IEEE Trans. Power Electron.*, accepted, 2021.

[5] J. Yin *et al*., "Variable Rounding Level Control Method for Modular Multilevel Converters," *IEEE Trans. Power Electron*., vol. 36, no. 4, pp. 4791-4801, Apr. 2021.

[6] P. Montero-Robina *et al*., "Feedforward Modulation Technique for More Accurate Operation of Modular Multilevel Converters," *IEEE Trans. Power Electron*., vol. 37, no. 2, pp. 1700-1710, Feb. 2022.

[7] C. Liu *et al*., "Submodule Capacitance Monitoring Strategy for Phase-Shifted Carrier Pulsewidth-Modulation-Based Modular Multilevel Converters," *IEEE Trans. Ind. Electron*., vol. 68, no. 9, pp. 8753-8767, Sep. 2021.

[8] M. Hagiwara, I. Hasegawa and H. Akagi, "Start-Up and Low-Speed Operation of an Electric Motor Driven by a Modular Multilevel Cascade Inverter," *IEEE Trans. Ind. Appl*., vol. 49, no. 4, pp. 1556-1565, Jul. /Aug. 2013.

[9] Z. Wang, J. Chen, K. Liao, J. Xiong, and K. Zhang, "Review on Low-frequency Ripple Suppression Methods for MMCs for Medium-voltage Drive Applications," *IET Power Electron*., vol. 11, no. 15, pp. 2403-2414, Dec. 2018.

[10] J. Kolb, F. Kammerer, M. Gommeringer and M. Braun, "Cascaded Control System of the Modular Multilevel Converter for Feeding Variable-Speed Drives," *IEEE Trans. Power Electron.*, vol. 30, no. 1, pp. 349-357, Jan. 2015.

[11] Y. Okazaki, H. Matsui, M. Hagiwara and H. Akagi, "Research trends of modular multilevel cascade inverter (MMCI-DSCC)-based medium-voltage motor drives in a low-speed range," in *Proc. ECCE ASIA*, Aug. 2014, pp. 1586-1593.

[12] S. Debnath, J. Qin and M. Saeedifard, "Control and Stability Analysis of Modular Multilevel Converter Under Low-Frequency Operation," *IEEE Trans. Ind. Electron*., vol. 62, no. 9, pp. 5329-5339, Sep. 2015.

[13] Y. Okazaki *et al*., "Experimental Comparisons Between Modular Multilevel DSCC Inverters and TSBC Converters for Medium-Voltage Motor Drives," *IEEE Trans. Power Electron.*, vol. 32, no. 3, pp. 1805-1817, Mar. 2017.

[14] B. Li, S. Zhou, D. Xu, D. Xu and W. Wang, "Comparative study of the sinusoidal-wave and square-wave circulating current injection methods for low-frequency operation of the modular multilevel converters," in *Proc. IEEE Energy Convers. Congr. Expo*., 2015, pp. 4700-4705.

[15] B. Li, S. Zhou, D. Xu, S. J. Finney and B. W. Williams, "A Hybrid Modular Multilevel Converter for Medium-Voltage Variable-Speed Motor Drives," *IEEE Trans. Power Electron.*, vol. 32, no. 6, pp. 4619-4630, Jun. 2017.

[16] S. Sau and B. G. Fernandes, "Modular Multilevel Converter Based Variable Speed Drive With Reduced Capacitor Ripple Voltage," *IEEE Trans. Ind. Electron*., vol. 66, no. 5, pp. 3412-3421, May. 2019.

[17] B. Li, Y. Zhang, G. Wang, W. Sun, D. Xu and W. Wang, "A Modified Modular Multilevel Converter With Reduced Capacitor Voltage Fluctuation," *IEEE Trans. Ind. Electron*., vol. 62, no. 10, pp. 6108-6119, Oct. 2015.

[18] Y. S. Kumar and G. Poddar, "Control of Medium-Voltage AC Motor Drive for Wide Speed Range Using Modular Multilevel Converter," *IEEE Trans. Ind. Electron*., vol. 64, no. 4, pp. 2742-2749, Apr. 2017.

[19] Y. S. Kumar and G. Poddar, "Medium-Voltage Vector Control Induction Motor Drive at Zero Frequency Using Modular Multilevel Converter," *IEEE Trans. Ind. Electron*., vol. 65, no. 1, pp. 125-132, Jan. 2018.

[20] M. Guan, B. Li, S. Zhou, Z. Xu and D. Xu, "Back-to-back hybrid modular multilevel converters for ac motor drive," in *Proc. Annu. Conf. IEEE Ind. Electron. Soc.*, 2017, pp. 1822-1827.

[21] B. Li, J. Hu, S. Zhou and D. Xu, "Hybrid back-to-back MMC system for variable speed AC machine drives," *CPSS Trans. Power Electron. and Appl*., vol. 5, no. 2, pp. 114-125, Jun. 2020.

[22] F. Deng, J. Hou, P. Jiang, H. Zhang, K. Zhu and Y. Hu, "Modular Multilevel Converter and Cycloconverter Based Machine Drive Systems," *in Proc. Annu. Conf. IEEE Ind. Electron. Soc*., 2020, pp. 5296-5301.

[23] B. R. Pelly, *Thyristor Phase-Controlled Converters and Cycloconverters*. New York: Willey-Interscience, 1971.

[24] Q. Tu, Z. Xu and L. Xu, "Reduced Switching-Frequency Modulation and Circulating Current Suppression for Modular Multilevel Converters," *IEEE Trans. Power Delivery*, vol. 26, no. 3, pp. 2009-2017, Jul. 2011.
[25] https://www.infineon.com/dgdl/Infineon-T2871N-DS-v05_00-EN.pdf?fileId=5546d46269e1c019016a5928cc753967
[26] P. A. Aravena, L. A. Morán, R. Burgos, P. Astudillo, C. Olivares and D. A. Melo, "High-Power Cycloconverter for Mining Applications: Practical Recommendations for Operation, Protection, and Compensation," *IEEE Trans. Ind. Appl*., vol. 51, no. 1, pp. 82-91, Jan. /Feb. 2015.
[27] F. Deng *et al*., "Capacitor ESR and C Monitoring in Modular Multilevel Converters," *IEEE Trans. Power Electron.*, vol. 35, no. 4, pp. 4063-4075, Apr. 2020.
[28] B. Li, Z. Xu, S. Shi, D. Xu and W. Wang, "Comparative Study of the Active and Passive Circulating Current Suppression Methods for Modular Multilevel Converters," *IEEE Trans. Power Electron.*, vol. 33, no. 3, pp. 1878-1883, Mar. 2018.

Yue Zhang was born in Shaanxi, China, in 1995. He received the B.Eng. degree in Smart Grid Information Engineering and the M.Sc. degree in Control Theory and Control Engineering from School of Automation, Nanjing University of Science and Technology, China, in 2017 and 2020, respectively. He is currently working toward the Ph.D. degree with the School of Electrical Engineering, Southeast University, Nanjing, China.

His main research interests include multilevel converters and machine drives.

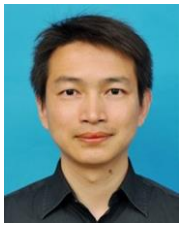

Fujin Deng (Senior Member, IEEE) received the B.Eng. degree in Electrical Engineering from China University of Mining and Technology, Jiangsu, China, in 2005, the M.Sc. Degree in Electrical Engineering from Shanghai Jiao Tong University, Shanghai, China, in 2008, and the Ph. D. degree in Energy Technology from the Department of Energy Technology, Aalborg University, Aalborg, Denmark, in 2012.

He joined the Southeast University in 2017 as a Professor in the School of Electrical Engineering, Southeast University, Nanjing, China. From 2013 to 2015 and from 2015 to 2017, he was a Postdoctoral Researcher and an Assistant Professor, respectively, in the Department of Energy Technology, Aalborg University, Aalborg, Denmark. His main research interests include wind power generation, multilevel converters, high-voltage direct-current technology, DC grid and offshore wind farm-power systems dynamics.

Jiehua Hou was born in Shanxi, China, in 1998. He received the B.Eng. degree in Electrical Engineering from School of Electrical Engineering, Southeast University, Nanjing, China, in 2020. He is currently working toward the M.Sc. degree in Electrical Engineering with Southeast University, Nanjing, China.

His main research interests include multilevel converters and machine drives.

Pengyuan Jiang was born in Jiangsu, China, in 1997. He received the B.Eng. degree in Electrical Engineering from School of Electrical Engineering, Southwest Jiaotong University, Sichuan, China, in 2019. He is currently pursuing the M.Sc. degree with the School of Electrical Engineering, Southeast University, Nanjing, China.

His main research interests include multilevel converters and machine drives.

Hanlu Zhang was born in Henan, China, in 1998. She received the B.Eng. degree in Electrical Engineering from School of Electrical Engineering, Southeast University, Nanjing, China, in 2020. She is currently working toward the M.Sc. degree in Electrical Engineering with Southeast University, Nanjing, China.

Her main research interests include multilevel converters and high-voltage direct-current technology.

Kangshun Zhu was born in Anhui, China, in 1999. He received the B. Eng. degree in Electrical Engineering from School of Electrical Engineering, Southeast University, Nanjing, China, in 2020. He is currently working toward the M.Sc. degree in Electrical Engineering with Southeast University, Nanjing, China.

His main research interests include multilevel converters and high-voltage direct-current technology.

Yihua Hu (Senior Member, IEEE) received the B.S. degree in electrical engineering in 2003, and the Ph.D. degree in power electronics and drives in 2011, both at China University of Mining and Technology. Between 2011 and 2013, he was with the College of Electrical Engineering, Zhejiang University as a Postdoctoral Fellow. Between 2013 and 2015, he worked as a Research Associate at the power electronics and motor drive group, the University of Strathclyde. Between 2016 and 2019, he was a Lecturer at the Department of Electrical Engineering and Electronics, University of Liverpool (UoL). Currently, he is a Reader at Electronics Engineering Department at The University of York (UoY). He has published over 120 papers in IEEE Transactions journals. His research interests include renewable generation, power electronics converters & control, electric vehicle, more electric ship/aircraft, smart energy system and non-destructive test technology. He is the associate editor of IEEE TRANSACTIONS ON INDUSTRIAL ELECTRONICS, *IET Renewable Power Generation, IET Intelligent Transport Systems* and *Power Electronics and Drives*. He is a fellow of Institution of Engineering and Technology (FIET). He was awarded Royal Society Industry Fellowship.

Sergio Vazquez (Fellow, IEEE) was born in Seville, Spain, in 1974. He received the M.S. and PhD degrees in industrial engineering from the University of Seville (US) in 2006, and 2010, respectively.

Since 2002, he is with the Power Electronics Group working in R\&D projects. He is an Associate Professor with the Department of Electronic Engineering, US. His research interests include power electronics systems, modeling, modulation, and control of power electronics converters applied to renewable energy technologies.

Dr. Vazquez was recipient as coauthor of the 2012 Best Paper Award of the IEEE TRANSACTIONS ON INDUSTRIAL ELECTRONICS and 2015 Best Paper Award of the *IEEE Industrial Electronics Magazine*. He is involved in the Energy Storage Technical Committee of the IEEE industrial electronics society and is currently serving as an Associate Editor of the IEEE TRANSACTIONS ON INDUSTRIAL ELECTRONICS.